

# ROBUST ESTIMATION OF BOUNDARY USING DOUBLY STOCHASTIC SCALING OF GAUSSIAN KERNEL

DHRUV KOHLI\*, JESSE HE†, CHESTER HOLTZ†, GAL MISHNE†, ALEXANDER CLONINGER\*†

**ABSTRACT.** This paper addresses the problem of detecting points on or near the boundary of a dataset sampled, potentially with noise, from a compact manifold with boundary. We extend recent advances in doubly stochastic scaling of the Gaussian heat kernel via Sinkhorn iterations to this setting. Our main contributions are: (a) deriving a characterization of the scaling factors for manifolds with boundary, (b) developing a boundary direction estimator, aimed at identifying boundary points, based on doubly stochastic kernel and local principal component analysis, and (c) demonstrating through simulations that the resulting estimates of the boundary points outperform the standard Gaussian kernel-based approach, particularly under noisy conditions.

**Keywords.** Manifold with boundary, doubly stochastic kernel, boundary detection.

## 1. INTRODUCTION

Given a set of points sampled, potentially with additive noise, from a compact manifold with boundary [19], we address the problem of identifying points on or near the boundary. The knowledge of such points is crucial for numerically solving partial differential equations with boundary conditions [26], unbiased kernel density estimation [23, 12, 15], constructing low-distortion local eigenmaps for regions near the boundary [13, 2, 3], and evaluating the performance of clustering algorithms [14] in preserving the structure within clusters.

Estimating the boundary of a data manifold is a relatively underexplored area. Berry and Sauer [1] proposed an estimation strategy aimed at the general case of data sampled from compact Riemannian manifolds in arbitrary dimensions. They employed the standard kernel density estimator (KDE) along with a boundary direction estimator (BDE) to numerically solve for the distances of the points from the boundary. In this work, we demonstrate that their standard Gaussian kernel-based estimates are highly sensitive to noise in the data. Similarly, Calder, Park, and Slepčev [6] introduced a boundary estimator that replaces the Gaussian kernel in KDE and BDE with a binary cutoff kernel. However, their method is only designed for (flat) Euclidean domains, as confirmed by our experiments. Moreover, we demonstrate that their method is also sensitive to noise.

A recent line of research [20, 18, 17, 8] investigated the concept of doubly stochastic scaling via Sinkhorn iterations [10] applied to the standard Gaussian heat kernel. These studies demonstrated that the doubly stochastic kernel leads to significant improvements in kernel density estimation on a closed manifold, and in approximating the eigenvectors of manifold Laplacian, especially in the presence of high-dimensional heteroskedastic and outlier-type noise. Additionally, Cheng and Landa [8] established convergence results for the bi-stochastically normalized Laplacian to a weighted manifold Laplacian and also demonstrated its resilience to outlier noise. This paper follows a similar approach by utilizing the doubly stochastic kernel to obtain robust boundary estimates for data points sampled from a manifold with noise. The contributions of our paper are as follows:

- (1) Similar to the characterization by Landa and Cheng [17], of the scaling factors  $\rho_h(\mathbf{x})$  that transform a Gaussian heat kernel  $k_h(\mathbf{x}, \mathbf{y})$  into a doubly stochastic kernel on a *closed manifold*, in this work, we derive a characterization of the scaling factors in the setting of a *manifold with*

---

\*Department of Mathematics, UC San Diego (dhkohli@ucsd.edu, acloninger@ucsd.edu)

†Halicioğlu Data Science Institute, UC San Diego (jeh020@ucsd.edu, chholtz@ucsd.edu, gmishne@ucsd.edu)

*boundary.* Our second-order characterization in Theorem 2.1 has the form:

$$A_h(\mathbf{x})\rho_h(\mathbf{x})^4q(\mathbf{x})^2 - B_h(x)\rho_h(\mathbf{x})^2q(\mathbf{x}) + \pi^d = \mathcal{O}(h^2)$$

where  $d$  is the dimension of the manifold,  $h$  is the Gaussian kernel bandwidth, and  $A_h(\mathbf{x})$  and  $B_h(\mathbf{x})$  depend on the distance  $b_{\mathbf{x}}$  of  $\mathbf{x}$  from the boundary, mean curvature induced by the boundary at  $\mathbf{x}$  and the derivative of the sampling density  $q(\mathbf{x})$  in the direction normal to the boundary at  $\mathbf{x}$ . Since the latter quantities are typically unknown for a given data manifold, for practical purposes, we obtain a relaxed first-order characterization in Corollary 2.4,

$$\rho_h(\mathbf{x})^2q(\mathbf{x}) = \zeta_h(\mathbf{x}) + \mathcal{O}(h)$$

where  $\zeta_h(\mathbf{x})$  depends only on the distance of  $\mathbf{x}$  from the boundary i.e. on  $b_{\mathbf{x}}$ .

- (2) We present a BDE  $\{\boldsymbol{\nu}_i\}_1^n$  by leveraging the doubly stochastic heat kernel  $\mathbf{W}$  and local principal component analysis (PCA). Precisely,

$$\boldsymbol{\nu}_i := \frac{1}{n-1} \sum_{j=1}^n \mathbf{W}_{ij} \tilde{\mathbf{U}}_i^T (\tilde{\mathbf{x}}_j - \tilde{\mathbf{x}}_i)$$

where the columns of  $\tilde{\mathbf{U}}_i \in \mathbb{R}^{m \times d}$  represent the  $d$  principal directions obtained by applying PCA in a neighborhood of the  $i$ -th point  $\tilde{\mathbf{x}}_i$ . In Theorem 3.1, we prove the convergence of  $\boldsymbol{\nu}_i$  to the normal direction to the boundary  $\boldsymbol{\eta}_{\mathbf{x}_i}$  up to a global factor that depends only on the distance to the boundary. To keep the focus of the paper on doubly stochastic scaling, our convergence analysis assumes access to the projector onto the tangent space. In our experiments, this projector is approximated using local PCA on noisy data points. With this assumption, we show that the following holds with high probability:

$$\boldsymbol{\nu}_i \xrightarrow{n \rightarrow \infty} h\beta_h(\mathbf{x})\boldsymbol{\eta}_{\mathbf{x}} + \mathcal{O}(h^2).$$

where  $\beta_h(\mathbf{x})$  depends solely on the distance  $b_{\mathbf{x}}$  of  $\mathbf{x}$  from the boundary. In fact,  $|\beta_h(\mathbf{x})|$  is a strictly decreasing function of  $b_{\mathbf{x}}$  and consequently, we are able to estimate the boundary points by simply thresholding the values of the normed<sup>1</sup> vectors  $\|\boldsymbol{\nu}_i\|$ . Our experimental results demonstrate that the doubly stochastic kernel and local PCA-based approach results in a significant improvement in boundary estimation compared to the standard Gaussian kernel-based approach [1], particularly in the presence of heteroskedastic noise.

The organization of the paper is as follows: in Section 1.1 we introduce the setup. In Section 2, we provide a characterization of the doubly stochastic scaling factors on manifolds with boundary. In Section 3, we present our boundary direction estimator and analyze its convergence. In Section 4, we showcase our experimental results demonstrating the effectiveness of our method, followed by conclusions in Section 5. Proofs of our results are provided in Section 6.

**1.1. Setup and Preliminaries.** Let  $\mathcal{M}$  be a  $d$ -dimensional compact Riemannian manifold with boundary  $\partial\mathcal{M}$  embedded in an  $m$ -dimensional Euclidean space. Let  $|\mathcal{M}|$  be the volume of  $\mathcal{M}$ ,  $\boldsymbol{\eta}_{\mathbf{x}}$  be the normal direction at  $\mathbf{x}$  to the boundary,  $H(\mathbf{x})$  be the mean curvature of the hypersurface parallel to  $\partial\mathcal{M}$  intersecting  $\mathbf{x}$  (which depends on the second fundamental form of  $\partial\mathcal{M} \subset \mathcal{M}$ ),  $b_{\mathbf{x}}$  denote the distance of  $\mathbf{x}$  from the boundary and  $dV(\mathbf{x})$  be the volume form of  $\mathcal{M}$  at  $\mathbf{x}$ .

Suppose  $(\mathbf{x}_i)_1^n \subset \mathbb{R}^m$  are sampled independently and identically from a smooth and positive probability distribution  $q(\mathbf{x})$  on  $\mathcal{M}$ . Let  $\tilde{\mathbf{x}}_i = \mathbf{x}_i + \boldsymbol{\varepsilon}(\mathbf{x}_i)$  be the observed samples where  $\{\boldsymbol{\varepsilon}(\mathbf{x}_i)\}_1^n \subset \mathbb{R}^m$  are independent, perhaps non-identical, sub-Gaussian random variables with zero mean and a sub-Gaussian norm of  $\|\boldsymbol{\varepsilon}(\mathbf{x}_i)\|_{\psi_2}$ . The noiseless setting is characterized by the constraint  $\boldsymbol{\varepsilon}(\mathbf{x}_i) = 0$

<sup>1</sup> $\|\cdot\|$  corresponds to the 2-norm throughout this work.

for all  $i \in 1, \dots, n$ . For  $h > 0$ , define the Gaussian kernel  $k_h$  and the affinity matrix  $\mathbf{K}_{ij}$  by

$$(1) \quad \begin{aligned} k_h(\tilde{\mathbf{x}}_i, \tilde{\mathbf{x}}_j) &:= e^{-\|\tilde{\mathbf{x}}_i - \tilde{\mathbf{x}}_j\|^2/h^2}, \\ \mathbf{K}_{ij} &:= \begin{cases} k_h(\tilde{\mathbf{x}}_i, \tilde{\mathbf{x}}_j) & i \neq j \\ 0 & i = j. \end{cases} \end{aligned}$$

Given the kernel matrix  $\mathbf{K}$ , the doubly stochastic matrix  $\mathbf{W} \in \mathbb{R}^{n \times n}$  is defined as in [20, 18] by

$$(2) \quad \mathbf{W}_{ij} = \mathbf{d}_i \mathbf{K}_{ij} \mathbf{d}_j \text{ and } \sum_{j=1}^n \mathbf{W}_{ij} = 1.$$

where  $\mathbf{d} \in \mathbb{R}^n$  are scaling factors. The existence of  $\mathbf{d}$  follows from [18] and these are obtained efficiently using Sinkhorn iterations [10]. In the continuous setting, these correspond to a positive function  $\rho_h$  on  $\mathcal{M}$  such that

$$(3) \quad \frac{1}{\pi^{d/2} h^d} \int_{\mathcal{M}} \rho_h(\mathbf{x}) k_h(\mathbf{x}, \mathbf{y}) \rho_h(\mathbf{y}) q(\mathbf{y}) dV(\mathbf{y}) = 1.$$

The existence of a smooth  $\rho_h$  on  $\mathcal{M}$  that satisfy the above constraint follows from [20, 16, 4]. In this work, we only need the following assumption:

(A1) There exists a positive scaling function  $\rho_h \in \mathcal{C}^3(\mathcal{M})$  that satisfies Eq. (3).

Under the sub-Gaussian noise setup, Landa and Cheng in [17] established a connection between the doubly stochastic kernel obtained from noisy observations and the Gaussian kernel obtained from clean samples. We are going to use their result and the underlying assumptions, as stated below, in the convergence analysis of our BDE in Section 3.

**Theorem 1.1** (Theorem 2.1 in [17]). *Under the assumptions:*

- (A2) *The sampling density  $q$  is positive and continuous on  $\mathcal{M}$ .*
- (A3)  *$\|\mathbf{x}\| \leq 1$  for all  $\mathbf{x} \in \mathcal{M}$ .*
- (A4) *There exists  $C > 0$  such that  $\max_{\mathbf{x} \in \mathcal{M}} \|\boldsymbol{\varepsilon}(\mathbf{x}_i)\|_{\psi_2} \leq C/(m^{1/4} \sqrt{\log m})$  for all  $\mathbf{x} \in \mathcal{M}$ .*
- (A5) *There exists  $\gamma > 0$  such that  $m \geq n^\gamma$  (this facilitates the analysis of doubly stochastic scaling in the large sample size and high dimension regime).*

the following holds,

$$(4) \quad \begin{aligned} \mathbf{W}_{i,j} &= \frac{\rho_h(\mathbf{x}_i) k_h(\mathbf{x}_i, \mathbf{x}_j) \rho_h(\mathbf{x}_j)}{(n-1) \pi^{d/2} h^d} (1 + \mathcal{E}_{i,j}) \\ \mathbf{d}_i &= \frac{\rho_h(\mathbf{x}_i)}{\sqrt{(n-1) \pi^{d/2} h^d}} e^{\frac{\|\boldsymbol{\varepsilon}(\mathbf{x}_i)\|^2}{h^2}} (1 + \mathcal{E}_{i,i}) \end{aligned}$$

where  $\mathcal{E}_{i,j} = \mathcal{O}_{m,n}^{(h)}(g(m,n))$ ,  $g(m,n) = g_0(n)$  in the noiseless setting and  $g(m,n) = \max\{g_0(n), g_1(m)\}$  otherwise. Here,

$$\begin{aligned} g_0(n) &:= \sqrt{\log n/n} \quad \text{and} \\ g_1(m) &:= \max\{m^{-1/4}, 1/\sqrt{\log m}\} \end{aligned}$$

and as defined in [17], a random variable  $X = \mathcal{O}_{m,n}^{(h)}(g(m,n))$  if there exist  $t_0, n_0(h), m_0(h), C(h) > 0$  such that for all  $n > n_0(h), m \geq m_0(h), \Pr\{|X| \leq tC(h)g(m,n)\} \geq 1 - n^{-t}$  for all  $t \geq t_0$ .

**Remark 1.1.** *The above result holds for continuous density  $q$ . However, we make the following stronger assumption throughout this work.*

(A2') *The sampling density  $q$  is positive and  $q \in \mathcal{C}^3(\mathcal{M})$ .*

## 2. CHARACTERIZING DOUBLY STOCHASTIC SCALING FACTORS ON MANIFOLDS WITH BOUNDARY

In [17], the authors characterized the scaling factors  $\rho_h(\mathbf{x})$  as defined in Eq. (3) in the setting of a closed manifold. Here, we obtain a characterization of  $\rho_h(\mathbf{x})$  on manifolds with boundary. First, we need the following lemmas: (a) on the third-order approximation of the integral against Gaussian kernel on a manifold with boundary [9, 25], and (b) on the directional derivative of the projection operator onto the tangent space.

**Lemma 2.1** (Theorem 4.7 in [25]). *Let  $\mathcal{M}$  be a compact  $d$ -dimensional  $\mathcal{C}^3$  Riemannian manifold with a  $\mathcal{C}^3$  boundary and a normal collar. Then for all  $f \in \mathcal{C}^3(\mathcal{M})$ ,  $\mathbf{x} \in \mathcal{M}$  and  $h$  sufficiently small,*

$$\begin{aligned} \frac{1}{h^d} \int_{\mathcal{M}} k_h(\mathbf{x}, \mathbf{y}) f(\mathbf{y}) dV(\mathbf{y}) &= m_h^{(0)}(\mathbf{x}) f(\mathbf{x}) + h m_h^{(1)}(\mathbf{x}) \left( \partial_{\boldsymbol{\eta}_{\mathbf{x}}} f(\mathbf{x}) + \frac{d-1}{2} H(\mathbf{x}) f(\mathbf{x}) \right) + \\ &\quad \frac{h^2}{2} \tilde{m}_2 \left( \tilde{\omega}(\mathbf{x}) f(\mathbf{x}) + \Delta f(\mathbf{x}) + \left( \frac{m_h^{(2)}(\mathbf{x})}{\tilde{m}_2} - 1 \right) \partial_{\boldsymbol{\eta}_{\mathbf{x}}}^2 f(\mathbf{x}) \right) + \mathcal{O}(h^3) \end{aligned}$$

where  $H(\mathbf{x})$  is the mean curvature of the hypersurface parallel to  $\partial\mathcal{M}$  intersecting  $\mathbf{x}$  (which depends on the second fundamental form of  $\partial\mathcal{M} \subset \mathcal{M}$ ),  $\tilde{\omega}(\mathbf{x})$  depends on the scalar curvature of  $\mathcal{M}$  and

$$(5) \quad m_\varepsilon^{(0)}(\mathbf{x}) := \frac{\pi^{d/2}}{2} \left( 1 + \operatorname{erf} \left( \frac{b_{\mathbf{x}}}{\varepsilon} \right) \right)$$

$$(6) \quad m_\varepsilon^{(1)}(\mathbf{x}) := -\frac{\pi^{(d-1)/2}}{2} e^{-b_{\mathbf{x}}^2/\varepsilon^2}$$

$$(7) \quad m_\varepsilon^{(2)}(\mathbf{x}) := \frac{b_{\mathbf{x}}}{\varepsilon} m_\varepsilon^{(1)}(\mathbf{x}) + \frac{m_\varepsilon^{(0)}(\mathbf{x})}{2}$$

$$(8) \quad \tilde{m}_2 = \int_{\mathbb{R}^d} \mathbf{z}_i^2 e^{-\|\mathbf{z}\|^2} d\mathbf{z} = \frac{\pi^{d/2}}{2}$$

In the following result, by applying Lemma 2.1 to Eq. (3), we derive the directional derivatives of the scaling factors  $\rho_h(\mathbf{x})$  and a quadratic equation in  $\rho_h^2(\mathbf{x})$  that characterizes the scaling factors on a manifold with boundary.

**Theorem 2.1.** *Let  $\mathcal{M}$  be a compact  $d$ -dimensional  $\mathcal{C}^3$  Riemannian manifold with a  $\mathcal{C}^3$  boundary and a normal collar. Suppose assumptions (A1) and (A2') hold:  $\rho_h \in \mathcal{C}^3(\mathcal{M})$  be a positive scaling function satisfying Eq. (3) and  $q \in \mathcal{C}^3(\mathcal{M})$  be the positive sampling density. Then the following hold.*

(I) *The derivative of  $\rho_h$  in the direction of  $\boldsymbol{\eta}_{\mathbf{x}}$  is,*

$$h \partial_{\boldsymbol{\eta}_{\mathbf{x}}} \rho_h(\mathbf{x}) = -\frac{2\rho_h(\mathbf{x})^3 (m_h^{(1)}(\mathbf{x}) q(\mathbf{x}) + h m_h^{(2)}(\mathbf{x}) \partial_{\boldsymbol{\eta}_{\mathbf{x}}} q(\mathbf{x}))}{\pi^{d/2} + 2m_h^{(2)}(\mathbf{x}) \rho_h(\mathbf{x})^2 q(\mathbf{x})} + \mathcal{O}(h^2)$$

Also, if  $\mathbf{v}_{\mathbf{x}} \in T_{\mathbf{x}}\mathcal{M}$  such that  $\mathbf{v}_{\mathbf{x}} \perp \boldsymbol{\eta}_{\mathbf{x}}$  then the derivative of  $\rho_h$  in the direction of  $\mathbf{v}_{\mathbf{x}}$  is,

$$\partial_{\mathbf{v}_{\mathbf{x}}} \rho_h(\mathbf{x}) = -\frac{\rho_h(\mathbf{x})^3 \partial_{\mathbf{v}_{\mathbf{x}}} q(\mathbf{x})}{(1 + \rho_h(\mathbf{x})^2 q(\mathbf{x}))} + \mathcal{O}(h).$$

(II)  $\rho_h(\mathbf{x})$  satisfies the following equation,

$$(9) \quad A_h(\mathbf{x}) \rho_h(\mathbf{x})^4 q(\mathbf{x})^2 - B_h(\mathbf{x}) \rho_h(\mathbf{x})^2 q(\mathbf{x}) + \pi^d = \mathcal{O}(h^2)$$

where  $A_h$  and  $B_h$  are defined as follows.

$$A_h(\mathbf{x}) = 2 \left\{ m_h^{(1)}(\mathbf{x})^2 - m_h^{(2)}(\mathbf{x}) \left( m_h^{(0)}(\mathbf{x}) + \frac{h(d-1)m_h^{(1)}(\mathbf{x})H(\mathbf{x})}{2} \right) \right\} \text{ and}$$



$$B_h(\mathbf{x}) = \pi^{d/2} m_h^{(1)}(\mathbf{x}) \left( h\omega(\mathbf{x}) - \frac{2b_{\mathbf{x}}}{h} \right),$$

where  $\omega(\mathbf{x}) := \frac{\partial_{\eta_{\mathbf{x}}} q(\mathbf{x})}{q(\mathbf{x})} + \frac{(d-1)}{2} H(\mathbf{x})$  depends on the sampling density and the mean curvature  $H(\mathbf{x})$  induced by the boundary at  $\mathbf{x}$ . Since  $\mathcal{M}$  is compact, the constant in  $\mathcal{O}(h^2)$  can be uniformly bounded over the manifold.

The proof of the above theorem, when specialized to closed and compact manifolds, results in the following corollary, which is reminiscent of the characterization of scaling factors presented in [17].

**Corollary 2.1.** *If  $\partial\mathcal{M} = \emptyset$  then*

$$\rho_h(\mathbf{x})^2 q(\mathbf{x}) = 1 + \mathcal{O}(h^2).$$

Moreover, the constant in  $\mathcal{O}(h^2)$  that depends on  $\mathbf{x}$  can be uniformly bounded since  $\mathcal{M}$  is compact.

In fact, for a sufficiently small  $h$  the above result holds within the interior of a manifold with nonempty boundary where  $b_{\mathbf{x}}/h \gg 0$ . The key component of the proof is the asymptotic expansion of the heat kernel in the interior of the manifold [25, 9], combined with the fact that when  $b_{\mathbf{x}}/h \rightarrow \infty$  then  $m_h^{(0)}(\mathbf{x}) \rightarrow \pi^{d/2}$ ,  $m_h^{(1)}(\mathbf{x}) \rightarrow 0$ ,  $\frac{b_{\mathbf{x}}}{h} m_h^{(1)}(\mathbf{x}) \rightarrow 0$  and  $m_h^{(2)}(\mathbf{x}) \rightarrow \pi^{d/2}/2$ . Consequently,  $A_h(\mathbf{x}) \rightarrow -\pi^d$  and  $B_h(\mathbf{x}) \rightarrow 0$  in Eq. (9). Thus  $\rho_h(\mathbf{x})^4 q(\mathbf{x})^2 \rightarrow 1 + \mathcal{O}(h^2)$ .

In addition to the cases of closed manifolds and the interior of a manifold with a boundary, a scenario where a second-order approximation of  $\rho_h(\mathbf{x})^2 q(\mathbf{x})$  can be easily described arises when  $H(\mathbf{x}) = 0$ , as with a flat boundary, and  $\partial_{\eta_{\mathbf{x}}} q(\mathbf{x}) = 0$ , as with a uniform sampling density. This is detailed in the corollary below.

**Corollary 2.2.** *If  $\partial\mathcal{M} \neq \emptyset$  and  $H(\mathbf{x}) = 0$ , then*

$$\rho_h(\mathbf{x})^2 q(\mathbf{x}) = C_h(\mathbf{x})(1 + \mathcal{O}(h^2)) \text{ where } C_h(\mathbf{x}) = \frac{B_h(\mathbf{x}) - \sqrt{B_h(\mathbf{x})^2 - 4\pi^d A_h(\mathbf{x})}}{2A_h(\mathbf{x})} > 0.$$

Moreover, if  $\partial_{\eta_{\mathbf{x}}} q(\mathbf{x}) = 0$  then  $C_h(\mathbf{x})$  only depends on  $b_{\mathbf{x}}$ , the distance of  $\mathbf{x}$  from the boundary.

In general, it seems challenging to obtain a second-order approximation of  $\rho_h(\mathbf{x})^2 q(\mathbf{x})$  that is independent of  $H(\mathbf{x})$  and  $\partial_{\eta_{\mathbf{x}}} q(\mathbf{x})$ , which are typically unknown for a given dataset. Even when  $\mathbf{x}$  lies on the boundary, the terms  $A_h(\mathbf{x})$  and  $B_h(\mathbf{x})$  depend on these quantities as shown in the corollary below.

**Corollary 2.3.** *If  $\partial\mathcal{M} \neq \emptyset$  then for  $\mathbf{x} \in \partial\mathcal{M}$  (i.e.  $b_{\mathbf{x}} = 0$ ),*

$$\begin{aligned} A_h(\mathbf{x}) &= \frac{\pi^{d-1}}{2} \left( 1 - \frac{\pi}{2} \right) + \frac{h(d-1)\pi^{d-1/2} H(\mathbf{x})}{8} \\ B_h(\mathbf{x}) &= -\frac{\pi^{d-1/2}}{2} h\omega(\mathbf{x}). \end{aligned}$$

Therefore, for practical purposes, we relax the result in Theorem 2.1 to obtain a first-order characterization of  $\rho_h(\mathbf{x})^2 q(\mathbf{x})$  that depends exclusively on  $b_{\mathbf{x}}$ , removing the reliance on  $H(\mathbf{x})$  and  $\partial_{\eta_{\mathbf{x}}} q(\mathbf{x})$ , that are not accessible for a given dataset.

**Corollary 2.4.** *If  $\partial\mathcal{M} \neq \emptyset$  then*

$$\rho_h(\mathbf{x})^2 q(\mathbf{x}) = \zeta_h(\mathbf{x}) + \mathcal{O}(h)$$

where

$$\zeta_h(\mathbf{x}) = \frac{\pi^{d/2}}{2} \frac{\frac{b_{\mathbf{x}}}{h} m_h^{(1)}(\mathbf{x}) + \sqrt{\left( \frac{b_{\mathbf{x}}}{h} m_h^{(1)}(\mathbf{x}) + m_h^{(0)}(\mathbf{x}) \right)^2 - 2m_h^{(1)}(\mathbf{x})^2}}{m_h^{(2)}(\mathbf{x})m_h^{(0)}(\mathbf{x}) - m_h^{(1)}(\mathbf{x})^2}$$

is a strictly decreasing convex function with a range of  $\left[2\sqrt{\frac{\pi}{\pi-2}}, 1\right)$ .

The above result will be utilized in the convergence proof of our doubly stochastic kernel-based BDE presented in Theorem 3.1 in the following section.

### 3. ESTIMATION OF BOUNDARY USING DOUBLY STOCHASTIC KERNEL

In this section, we first review the standard Gaussian kernel-based BDE proposed in [1] and how it is utilized to estimate the boundary points. Next, we propose a BDE that leverages the doubly stochastic kernel obtained through Sinkhorn iterations [17, 10] applied to the Gaussian kernel, and local PCA. Using Theorem 2.1 and Corollary 2.4 we establish the convergence of our BDE to the normal direction to the boundary, up to a factor that depends only on the distance to the boundary. Building on this result, we introduce a straightforward algorithm for computing boundary points of the given data manifold.

**3.1. Boundary estimation using standard Gaussian kernel.** Using the standard Gaussian kernel  $\mathbf{K}_{ij}$  as defined in Eq. (1), Berry and Sauer [1] defined a KDE  $f$  and a BDE  $\boldsymbol{\mu}$  as follows,

$$(10) \quad \begin{aligned} f_i &:= \frac{1}{n-1} \sum_{j=1}^n \mathbf{K}_{ij} \\ \boldsymbol{\mu}_i &:= \frac{1}{n-1} \sum_{j=1}^n \mathbf{K}_{ij} (\tilde{\mathbf{x}}_j - \tilde{\mathbf{x}}_i). \end{aligned}$$

Intuitively,  $\boldsymbol{\mu}_i$  vanishes in the interior while, near the boundary, it is non-zero and points in the direction of  $-\boldsymbol{\eta}_{\mathbf{x}_i}$ , as illustrated in Figure 1.

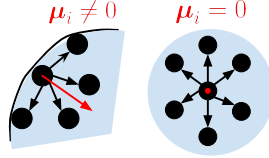


FIGURE 1. A schematic illustrating  $\boldsymbol{\mu}_i$  at the boundary and in the interior.

Berry and Sauer [1] showed in the noiseless setting that  $\boldsymbol{\mu}_i$  converges to the normal direction  $-\boldsymbol{\eta}_{\mathbf{x}_i}$  up to a global factor that depends on the distance  $b_{\mathbf{x}_i}$  of  $\mathbf{x}_i$  from the boundary and the sampling density  $q(\mathbf{x}_i)$  at  $\mathbf{x}_i$ . They also showed that  $f_i$  converges to the sampling density  $q(\mathbf{x}_i)$  up to another global factor that depends on  $b_{\mathbf{x}_i}$ . Precisely,

$$(11) \quad \begin{aligned} \mathbb{E}[f_i] &= h^d m_h^{(0)}(\mathbf{x}_i) q(\mathbf{x}_i) (1 + \mathcal{O}(h)) \text{ and} \\ \mathbb{E}[\boldsymbol{\mu}_i] &= h^{d+1} \boldsymbol{\eta}_{\mathbf{x}_i} q(\mathbf{x}_i) m_h^{(1)}(\mathbf{x}_i) (1 + \mathcal{O}(h)). \end{aligned}$$

Taking the ratio of  $\mathbb{E}[f_i]$  and  $\|\mathbb{E}[\boldsymbol{\mu}_i]\|$  and thereby eliminating  $q(\mathbf{x}_i)$ , they obtain

$$\frac{h\mathbb{E}[f_i]}{\sqrt{\pi} \|\mathbb{E}[\boldsymbol{\mu}_i]\|} = \frac{m_h^{(0)}(\mathbf{x}_i) (1 + \mathcal{O}(h))}{\sqrt{\pi} |m_h^{(1)}(\mathbf{x}_i)|} = \left(1 + \operatorname{erf}\left(\frac{b_{\mathbf{x}_i}}{h}\right)\right) e^{b_{\mathbf{x}_i}^2/h^2} (1 + \mathcal{O}(h)).$$

They finally estimated the distances to the boundary  $\hat{b}_{\mathbf{x}_i}$  by finding the root of the equation  $F(b_{\mathbf{x}}) = h f_i / \sqrt{\pi} \|\boldsymbol{\mu}_i\|$  using Newton's method where  $F(b_{\mathbf{x}}) = \left(1 + \operatorname{erf}\left(\frac{b_{\mathbf{x}}}{h}\right)\right) e^{b_{\mathbf{x}}^2/h^2}$ .

**3.2. Boundary estimation using doubly stochastic kernel and local PCA.** We propose a BDE by combining the the doubly stochastic kernel [17] and local PCA as follows,

$$(12) \quad \boldsymbol{\nu}_i := \frac{1}{n-1} \sum_{j=1}^n \mathbf{W}_{ij} \tilde{\mathbf{U}}_i^T (\tilde{\mathbf{x}}_j - \tilde{\mathbf{x}}_i).$$

Here,  $\tilde{\mathbf{U}}_i \in \mathbb{R}^{m \times d}$  serves as an approximation of an orthogonal basis of  $T_{\mathbf{x}_i}\mathcal{M}$  and is obtained by applying PCA on a neighborhood of  $\tilde{\mathbf{x}}_i$ . Unlike the Gaussian kernel-based approach [1], which utilizes vectors  $\tilde{\mathbf{x}}_j - \tilde{\mathbf{x}}_i$  between the original (potentially noisy) data points, our method employs vectors between the PCA-projected points,  $\tilde{\mathbf{U}}_i^T(\tilde{\mathbf{x}}_j - \tilde{\mathbf{x}}_i)$ . At a high level, this design leverages the noise-resilient properties of the doubly stochastic kernel [17, 8] combined with the denoising capabilities of local PCA [11].

To maintain the focus of this paper on the doubly stochastic scaling and to simplify our analysis, we adopt the following assumptions in addition to (A1, A2', A3-A5):

- (A6) The projector onto the tangent space is assumed to be available. Specifically, we assume access to the matrices  $\{\mathbf{U}_i\}_1^n \subset \mathbb{R}^{m \times d}$ , where the columns of  $\mathbf{U}_i$  form an orthonormal basis of  $T_{\mathbf{x}_i}\mathcal{M}$ . In our experiments, however, we approximate an orthonormal basis of  $T_{\mathbf{x}_i}\mathcal{M}$  using  $\tilde{\mathbf{U}}_i$ , obtained by applying local PCA to noisy observations. For readers interested in the analysis showing that  $\tilde{\mathbf{U}}_i$  is close to a true basis  $\mathbf{U}_i\mathbf{S}_i$  for some  $\mathbf{S}_i \in \mathbb{O}(d)$ , we refer to the following papers [22, 24, 7, 27].
- (A7) The noise  $\varepsilon(\mathbf{x}_i)$  is orthogonal to the tangent space i.e.  $\mathbf{U}_i^T \varepsilon(\mathbf{x}_i) = 0$ .

With assumptions (A6) and (A7), we are now ready to state our main result, which characterizes our BDE  $\boldsymbol{\nu}_i$ .

**Theorem 3.1.** *Under assumptions (A1, A2', A3-A7), we have*

$$(13) \quad \boldsymbol{\nu}_i = h\beta_h(\mathbf{x})\boldsymbol{\eta}_{\mathbf{x}} + \mathcal{O}(h^2) + \mathcal{O}^{(h)}(g(m, n))$$

where  $\mathcal{O}^{(h)}(g(m, n))$  is defined in Theorem 1.1 and

$$\beta_h(\mathbf{x}) = \frac{m_h^{(1)}(\mathbf{x})\zeta_h(\mathbf{x})}{\pi^{d/2} + 2m_h^{(2)}(\mathbf{x})\zeta_h(\mathbf{x})}.$$

Here,  $-\beta_h(\mathbf{x})$  is a positive and strictly decreasing convex function that depends only on  $b_{\mathbf{x}}$ , the distance from  $\mathbf{x}$  from the boundary, and decays from  $\frac{1}{2}(\sqrt{\pi} - \sqrt{\pi - 2})$  to 0 as  $b_{\mathbf{x}}$  goes from 0 to  $\infty$ .

If the sampling density is uniform, then the convergence order improves from  $\mathcal{O}(h^2)$  to  $\mathcal{O}(h^3)$ .

**Corollary 3.1.** *Under assumptions (A1, A2', A3-A7), if  $q$  is uniform i.e.  $q = 1/|\mathcal{M}|$ , we have*

$$\boldsymbol{\nu}_i = h\beta_h(\mathbf{x})\boldsymbol{\eta}_{\mathbf{x}} + \mathcal{O}(h^3) + \mathcal{O}^{(h)}(g(m, n)).$$

The proof follows directly from the proof of Theorem 3.1 by substituting zeros for the partial derivatives of  $q$ . From the above results, it follows that

$$\|\boldsymbol{\nu}_i\| \approx h|\beta_h(\mathbf{x}_i)| = -h\beta_h(\mathbf{x}_i)$$

for sufficiently small  $h$ , with high probability in the large sample and high-dimensional setting. Since  $\beta_h(\mathbf{x})$  depends solely on  $b_{\mathbf{x}}$  and is strictly decreasing, we can identify the boundary points by simply thresholding  $\{\|\boldsymbol{\nu}_i\|\}_1^n$ , for example by using a chosen percentile of these values. The steps to compute  $(\boldsymbol{\nu}_i)_1^n$  are summarized in Algorithm 1, and it differs from the Gaussian kernel-based approach described in Section 3.1 in two ways: (i) it employs Sinkhorn iterations [10, 17] to construct the doubly stochastic kernel, and (ii) it eliminates the need for KDE computations and Newton's method to approximate boundary points.

**Algorithm 1** Boundary direction estimator**Require:**  $(\tilde{\mathbf{x}}_i)_1^n \subset \mathbb{R}^m$ ,  $d, h, k_{\text{nn}}$ .

- 1: Construct  $\mathbf{K}$  as in Eq. (1).
- 2: Construct  $\mathbf{W}$  as in Eq. (2) using Sinkhorn iterations [10, 17].
- 3: **for**  $i = 1 \rightarrow n$  **do**
- 4:    $\tilde{\mathcal{N}}_i \leftarrow k_{\text{nn}}$ -nearest neighbors of  $\tilde{\mathbf{x}}_i$ .
- 5:    $\tilde{\mathbf{U}}_i \leftarrow$  PCA on  $\{\tilde{\mathbf{x}}_j : j \in \tilde{\mathcal{N}}_i\}$ .
- 6:   Set  $\boldsymbol{\nu}_i = \frac{1}{n-1} \sum_{j=1}^n \mathbf{W}_{ij} \tilde{\mathbf{U}}_i^T (\tilde{\mathbf{x}}_j - \tilde{\mathbf{x}}_i)$ .
- 7: **end for**

## 4. EXPERIMENTS

In Sections 4.1 and 4.2, we estimate points located on and near the boundary for data uniformly sampled from two geometries: (a) a circular annulus and (b) a curved truncated torus. These estimations are conducted under three noise scenarios: no noise, homoskedastic noise, and heteroskedastic noise. Additionally, in Section 4.3, we identify images in the MNIST dataset that lie close to and far from the boundary. We evaluate the performance of the following methods for boundary estimation:

- (1) The standard Gaussian heat kernel as in Section 3.1, and a local PCA enhanced variant. In the latter, during the calculation of  $\boldsymbol{\mu}_i$  in Eq. (10),  $\tilde{\mathbf{x}}_j - \tilde{\mathbf{x}}_i$  is replaced with  $\tilde{\mathbf{U}}_i^T (\tilde{\mathbf{x}}_j - \tilde{\mathbf{x}}_i)$  as in Eq. (12), by employing local PCA in a small neighborhood around  $\tilde{\mathbf{x}}_i$ . These methods are denoted as **Gaussian** and **Gaussian+LPCA**, respectively.
- (2) The doubly stochastic kernel with local PCA as in Algorithm 1, and a variant of it which, while calculating  $\boldsymbol{\nu}_i$  in Eq. (12), directly uses the difference in the observations  $\tilde{\mathbf{x}}_j - \tilde{\mathbf{x}}_i$  as in Eq. (10), instead of the local PCA projections. These methods are referred to as **DS+LPCA** and **DS**, respectively.
- (3) The method proposed in [6] that estimates the boundary using an approach similar to **Gaussian**, but replaces the Gaussian kernel with a binary cutoff kernel. We refer to this method as **Binary**. The implementation of this method is available in [5].

To estimate the boundary, we threshold the estimated distances  $(\hat{b}_{\mathbf{x}_i})_1^n$  and the norm of BDE  $(\|\boldsymbol{\nu}_i\|)_1^n$  based on a specified percentile. For clarity, we define the ground truth  $p$ -th percentile boundary as

$$(14) \quad \mathcal{B}_p = \{\mathbf{x}_k : b_{\mathbf{x}_k} \leq p\text{-th percentile of } (b_{\mathbf{x}_i})_1^n\}$$

and the estimated  $p$ -th percentile boundary as

$$(15) \quad \hat{\mathcal{B}}_p = \begin{cases} \{\mathbf{x}_k : \hat{b}_{\mathbf{x}_k} \leq p\text{-th percentile of } (\hat{b}_{\mathbf{x}_i})_1^n\} & \text{with Gaussian, Gaussian+LPCA \& Binary} \\ \{\mathbf{x}_k : \|\boldsymbol{\nu}_k\| \geq (100 - p)\text{th percentile of } (\|\boldsymbol{\nu}_i\|)_1^n\} & \text{with DS \& DS+LPCA.} \end{cases}$$

To measure the discrepancy between the estimated and true boundaries, we use the Jaccard index,

$$(16) \quad \mathcal{J}_p = \frac{|\mathcal{B}_p \cap \hat{\mathcal{B}}_p|}{|\mathcal{B}_p \cup \hat{\mathcal{B}}_p|}.$$

The code is available at [https://github.com/chiggum/robust\\_boundary\\_estimation](https://github.com/chiggum/robust_boundary_estimation).

**4.1. Data descriptions.** For our first set of datasets, we generate  $n = 7076$  uniformly distributed points in  $\mathbb{R}^2$ , sampled as  $\{(r_i \cos(\theta_i), r_i \sin(\theta_i))\}_1^n$  from a circular annulus with an outer radius of 1 and an inner radius of 0.3, i.e.  $r_i \in [0.3, 1]$  and  $\theta_i \in (-\pi, \pi]$  (see Figure 2). We then project these points into  $m = 2000$  dimensions using an orthogonal transformation. This forms our noiseless dataset. Let  $\mathcal{S}$  be the 2-dimensional subspace containing the annulus. We construct two noisy variants of the data (a) by adding homoskedastic noise in a ball of radius 0.2 at each point, ensuring that the noise is orthogonal to  $\mathcal{S}$  (this preserves the ground truth distances of the

points from the boundary for evaluation) and (b) by adding heteroskedastic noise in a ball of radius  $0.01 + 0.2(1 + \cos(2\theta_i))/2$  at each point, also orthogonal to  $\mathcal{S}$ . The noise distribution is illustrated in Figure 2.

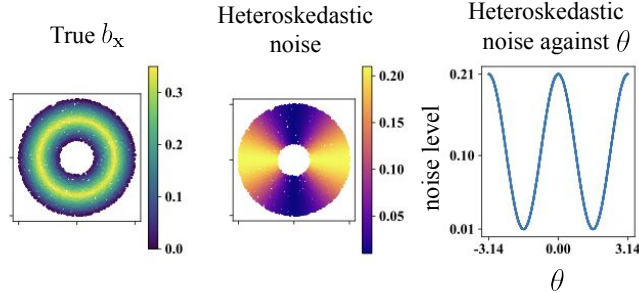


FIGURE 2. From left to right: (i) the true distances of uniformly sampled points from the boundary of the circular annulus, (ii) the noise levels visualized on the annulus, and (iii) the noise levels plotted as a function of the angular coordinate  $\theta$  of the data points.

For our second set of datasets, we generate  $n = 6163$  uniformly distributed points

$$\{(R + r \cos(\theta_i)) \cos(\phi_i), (R + r \cos(\theta_i)) \sin(\phi_i), r \sin(\theta_i)\}_1^n$$

on a curved torus in  $\mathbb{R}^3$  where  $R = 0.25$ ,  $r = 1/4\pi^2 R$ ,  $\theta_i \in [0, 2\pi)$  and  $\phi_i \in [0, 2\pi)$ . The torus is then truncated by removing points with  $x$ -coordinate greater than 0.18, as shown in Figure 3. These points are projected into  $m = 2000$  dimensions using an orthogonal transformation, forming our noiseless dataset. Let  $\mathcal{S}$  represent the 3-dimensional subspace containing the truncated torus. We generate two noisy variants of the data (a) by adding homoskedastic noise in a ball of radius 0.075 at each point while ensuring that the noise is orthogonal to  $\mathcal{S}$  and (b) by adding heteroskedastic noise in a ball of radius  $0.01 + 0.075(1 + \cos(2\theta_i))/2$  at each point, also orthogonal to  $\mathcal{S}$ . The noise distribution is illustrated in Figure 3.

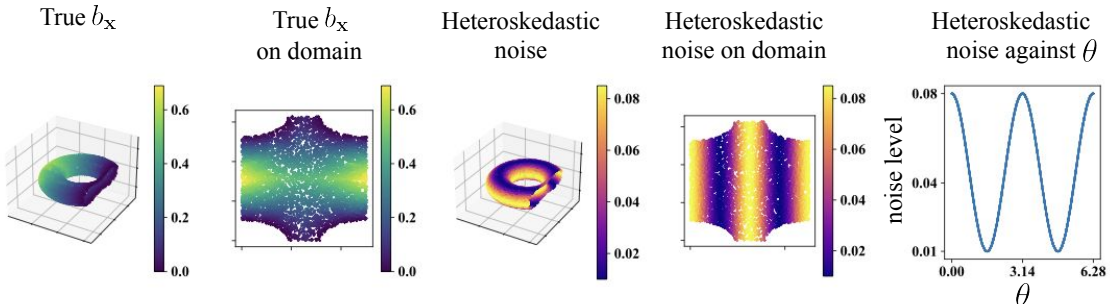


FIGURE 3. From left to right: (i) true distances of uniformly distributed points from the boundary of a truncated torus, (ii) true distances to the boundary visualized on the two-dimensional domain of the truncated torus, (iii) noise level illustrated on the truncated torus, (iv) noise level visualized on the domain, and (v) noise level as a function of the angular coordinate  $\theta$  of the data points.

**4.2. Interpreting results.** For both datasets, we construct the standard Gaussian kernel and the doubly stochastic kernel [17] using a bandwidth of  $h = 0.1$ . Using these kernels,  $d = 2$  and  $k_{nn} = 256$  neighbors for local PCA computations, we estimate the distances to the boundary using DS+LPCA, DS, Gaussian+LPCA and Gaussian. We use the same number of nearest neighbors while estimating distances to boundary using Binary. Subsequently we compute the  $p$ -th percentile boundary  $\hat{\mathcal{B}}_p$  (Eq. (15)) for each method. To compare the performance, we calculate the Jaccard index  $\mathcal{J}_p$  (Eq. (16)) against the ground truth boundary  $\mathcal{B}_p$  (Eq. (14)) for various values of  $p$ . The results are presented in Figures 4 to 6, and we summarize key observations from the figures below.

(1) Noiseless setting:

- (a) Since the circular annulus is flat, local PCA has no impact. As a result, **DS+LPCA** and **DS** achieve identical Jaccard indices, while **Gaussian+LPCA** and **Gaussian** also perform equivalently. All the methods seem to achieve similar performance while the **Binary** method has slightly better performance. The slightly better performance of **DS** over **Gaussian** can be attributed to the norm of the BDE,  $\|\nu_i\|$  in Eq. (12) and  $\|\mu_i\|$  in Eq. (10). The BDE norm is expected to be zero in the interior and non-zero near the boundary of the manifold (see Figures 1 and 6). However, **Gaussian** frequently yields non-zero BDE, whereas **DS** maintains the BDE close to zero within the annulus interior.
  - (b) The curvature of the torus makes local PCA an important factor. We observe that **DS+LPCA** and **Gaussian+LPCA** achieve comparable performance and outperform **DS** and **Gaussian**, indicating that local PCA enhances the accuracy of boundary estimation. At the same time, the performance of **Binary** degrades significantly, suggesting the method is sensitive to the curvature. This is consistent with the observation in [6] that the method **Binary** is designed for Euclidean domains, not general smooth manifolds.
- (2) Under homoskedastic noise: For both the circular annulus and the truncated torus, the Jaccard index for **DS+LPCA**, **DS**, and **Gaussian+LPCA** remains robust against noise, whereas the performance of **Gaussian** and **Binary** deteriorates significantly. The degradation of **Gaussian** can be attributed to the behavior of the BDE observed in Figure 6 where the BDE from **Gaussian** is completely corrupted by noise. Specifically, the BDE is relatively large in the interior and smaller at the boundary, contrary to the expected trend as illustrated in Figure 1. In fact, the norm of the BDE is so large that the estimated  $\hat{b}_{\mathbf{x}_i}$  collapse to zero (due to Newton’s method converging to negative values that are clipped to zero), resulting in degenerate boundary in Figure 4.

Interestingly, while the norm of the BDE for **DS** increases in the interior compared to the noiseless case, the boundary values remain relatively higher. This ensures that the estimates  $\|\nu_i\|$  at the boundary are higher than those in the interior, enabling more accurate estimates of boundary points. Lastly, as shown in Figure 6, **DS+LPCA** and **Gaussian+LPCA** exhibit similar BDE values, leading to comparable boundary estimates as shown in Figure 4, consistent with the noiseless case. This again highlights that incorporating local PCA significantly enhances the accuracy of boundary estimation, as evidenced by the substantial increase in the Jaccard index from **Gaussian** to **Gaussian+LPCA**.

- (3) Under heteroskedastic noise: For both the circular annulus and the truncated torus, **DS+LPCA** yields significantly high Jaccard index compared to **Gaussian+LPCA**, while the performance of **DS** deteriorates significantly. In fact, **Gaussian** and **DS** identify the points in the regions with high noise levels (see Figures 2 and 3 for noise distributions) as the boundary points as shown in Figures 4 and 5. This is again attributed to the corruption of BDE due to noise as shown in Figure 6. Although the BDE for **Gaussian+LPCA** is also affected by heteroskedastic noise, the impact is less pronounced compared to **DS** and **Gaussian**. Nonetheless, the noise still leads to inaccuracies in the boundary estimates as shown in Figures 4 and 5. In contrast, the BDE for **DS+LPCA** shows greater resilience to noise, indicating that both doubly stochastic scaling and local PCA are crucial for producing robust boundary estimates.

**4.3. MNIST.** In this experiment, we start by randomly selecting 5000 images of size  $28 \times 28$  for each of the 10 digits in the MNIST dataset, resulting in 10 datasets, each containing  $n = 5000$  samples in  $m = 784$  dimensions. For each dataset, the median distance to the 128th nearest neighbor of each image is used as the bandwidth  $h$ , and the local PCA is computed using  $k_{\text{nn}} = 512$  and  $d = 2$ . Using **DS**, **DS+LPCA**, and **Gaussian+LPCA**, we compute the 10th percentile boundary,  $\hat{\mathcal{B}}_{10}$ , as defined in Eq. (15). These results are visualized on a two-dimensional UMAP [21] embedding of the entire dataset in Figure 7. It is important to note that the boundary estimation is performed on the raw datasets, not the UMAP embeddings.

Consistent with our simulations on synthetic datasets, the boundary estimated by **DS** and **Binary** are highly noisy, with a Jaccard index of 0.257 and 0.083 respectively, when compared to the

boundary estimated by DS+LPCA. Note that there is no ground-truth boundary in this context, and unlike the scenarios in previous sections, the Jaccard index here serves to quantify the qualitative differences between the methods. From Figure 7, it is evident that DS and Binary misclassify numerous points as being close to the boundary. In contrast, the boundaries computed using DS+LPCA and Gaussian+LPCA have a significant overlap, with a Jaccard index of 0.847. However, there are subtle differences. As shown in Figure 7, points that lie on the boundary estimated by DS+LPCA but not on the one by Gaussian+LPCA tend to be more dispersed along the boundary, while Gaussian+LPCA identifies points that are more concentrated in tightly packed regions resembling corners in the embedding, as is evident for digits 3, 5, 7, and 9. This suggests that Gaussian+LPCA provides a skewed boundary estimate than DS+LPCA, resulting in boundary points localized within specific regions.

Finally, to examine the differences between images near and far from the boundary, we randomly sampled 15 images from  $\widehat{\mathcal{B}}_5$  and outside  $\widehat{\mathcal{B}}_{95}$ , as estimated using DS+LPCA. The former set represents images near the boundary, while the latter represents images in the interior. These images are visualized in Figure 8. Clearly, images within the interior exhibit less variation, whereas those near the boundary display greater variation. The contrast is evident in the average of the 15 images per digit, displayed in the last columns of Figure 8. This highlights that the boundary points capture more diverse and nuanced features of the dataset, emphasizing the importance of accurately identifying them. Furthermore, this insight opens new avenues for exploring the computational benefits and generalization performance of machine learning models trained solely on boundary points rather than on the entire dataset.

## 5. CONCLUSION

In this work, we have developed a robust framework for detecting boundary points for data sampled from a manifold with boundary and in the presence of noise. To accomplish this, we extended the recent results in doubly stochastic scaling of the Gaussian kernel [20, 18, 17, 8] on closed manifolds to the setting of manifolds with boundaries. Specifically, we obtained a novel characterization of the scaling factors that transform a Gaussian kernel into a doubly stochastic kernel on manifolds with boundary. We further developed a BDE leveraging the doubly stochastic kernel along with local PCA, and utilized our characterization of scaling factors to prove its convergence.

Our experiments demonstrated that our proposed BDE significantly improves the detection of boundary points compared to the standard Gaussian and binary kernel-based methods [1, 6], particularly in noisy conditions (Figures 4 to 6). Our simulations underline the importance of incorporating both doubly stochastic scaling and local PCA for robust performance. Additionally, we observed that boundary points capture a wider range of features within the data (Figure 8). In future work, we aim to assess the trade-off between training models exclusively on boundary points versus the full dataset. This includes exploring the impact on model performance, computational efficiency, and generalization capabilities.

## 6. PROOFS

The following definition and lemma are needed for the proofs that follow. Let  $\Pi_{\mathbf{x}} : \mathcal{M} \mapsto T_{\mathbf{x}}\mathcal{M}$  be the projector onto the tangent space at  $\mathbf{x}$ . Define

$$\mathcal{P}_{\mathbf{x}}(\mathbf{y}) := \Pi_{\mathbf{x}}(\mathbf{y}) - \mathbf{x}.$$

**Lemma 6.1.** For  $\mathbf{v}_{\mathbf{x}} \in T_{\mathbf{x}}\mathcal{M}$  and  $\partial_{\mathbf{v}_{\mathbf{x}}} = \partial/\partial\mathbf{v}_{\mathbf{x}}$ ,

$$\mathcal{P}_{\mathbf{x}}(\mathbf{x}) = 0, \quad \partial_{\mathbf{v}_{\mathbf{x}}}\mathcal{P}_{\mathbf{x}}(\mathbf{x}) = \mathbf{v}_{\mathbf{x}} \quad \text{and} \quad \partial_{\mathbf{v}_{\mathbf{x}}}^2\mathcal{P}_{\mathbf{x}}(\mathbf{x}) = 0.$$

**Proof of Lemma 6.1.** Let  $(\partial_i)_1^d$  be an orthonormal basis of  $T_{\mathbf{x}}\mathcal{M}$ . Then there exist  $a^i \in \mathbb{R}$  and  $b^i : \mathcal{M} \mapsto \mathbb{R}$  for all  $i \in [1, d]$  such that  $\mathbf{v}_{\mathbf{x}} = a^i\partial_i$  (using Einstein notation) and  $\mathcal{P}_{\mathbf{x}}(\mathbf{y}) = b^i(\mathbf{y})\partial_i$ .

Moreover,  $b^i(\mathbf{x}) = 0$  for all  $i \in [1, d]$ ,

$$\begin{aligned}\partial_j b^i(\mathbf{y}) &= \delta_j^i + \mathcal{O}(\|\mathbf{x} - \mathbf{y}\|^2) \text{ and} \\ \partial_k \partial_j b^i(\mathbf{y}) &= \mathcal{O}(\|\mathbf{x} - \mathbf{y}\|).\end{aligned}$$

Thus,  $\mathcal{P}_{\mathbf{x}}(\mathbf{x}) = 0$  is trivial. Then

$$\begin{aligned}\partial_{\mathbf{v}_{\mathbf{x}}} \mathcal{P}_{\mathbf{x}}(\mathbf{x}) &= a^j \partial_j b^i(\mathbf{x}) \partial_i = a^j \delta_j^i \partial_i = a^i \partial_i = \mathbf{v}_{\mathbf{x}}, \\ \partial_{\mathbf{v}_{\mathbf{x}}}^2 \mathcal{P}_{\mathbf{x}}(\mathbf{x}) &= \mathbf{v}_{\mathbf{x}}(\mathbf{v}_{\mathbf{x}} \mathcal{P}_{\mathbf{x}})(\mathbf{x}) = \mathbf{v}_{\mathbf{x}}(a^j \partial_j b^i)(\mathbf{x}) \partial_i = a^k a^j \partial_k \partial_j b^i(\mathbf{x}) \partial_i = 0\end{aligned}$$

**Proof of Theorem 2.1.** For brevity, we use the following shorthand notation for the proof:  $\rho \equiv \rho_h(\mathbf{x})$ ,  $q \equiv q(\mathbf{x})$ ,  $H \equiv H(\mathbf{x})$ ,  $\omega \equiv \omega(\mathbf{x})$ ,  $A \equiv A_h(\mathbf{x})$ ,  $B \equiv B_h(\mathbf{x})$ ,  $m_i \equiv m_h^{(i)}(\mathbf{x})$  for  $i = 1, 2$  and 3.

For part (I), take the derivative of Eq. (3) with respect to  $\mathbf{x}$  in the direction of  $\mathbf{v}_{\mathbf{x}} \in T_{\mathbf{x}}\mathcal{M}$ ,

$$\int_{\mathcal{M}} (k_h(\mathbf{x}, \mathbf{y}) \partial_{\mathbf{v}_{\mathbf{x}}} \rho_h(\mathbf{x}) + \rho_h(\mathbf{x}) \partial_{\mathbf{v}_{\mathbf{x}}} k_h(\mathbf{x}, \mathbf{y})) \rho_h(\mathbf{y}) q(\mathbf{y}) dV(\mathbf{y}) = 0.$$

Using  $\partial_{\mathbf{v}_{\mathbf{x}}} k_h(\mathbf{x}, \mathbf{y}) = 2k_h(\mathbf{x}, \mathbf{y}) \mathbf{v}_{\mathbf{x}}^T \mathcal{P}_{\mathbf{x}}(\mathbf{y}) / h^2$  and Eq. (3) followed by Lemmas 2.1 and 6.1,

$$(17) \quad \pi^{d/2} \frac{\partial_{\mathbf{v}_{\mathbf{x}}} \rho}{\rho} + \frac{2m_1 \rho^2 q}{h} \frac{\mathbf{v}_{\mathbf{x}}^T \boldsymbol{\eta}_{\mathbf{x}}}{h} + 2\tilde{m}_2 \rho \left( q \partial_{\mathbf{v}_{\mathbf{x}}} \rho + \rho \partial_{\mathbf{v}_{\mathbf{x}}} q + \left( \frac{m_2}{\tilde{m}_2} - 1 \right) \partial_{\boldsymbol{\eta}_{\mathbf{x}}}(\rho q) \mathbf{v}_{\mathbf{x}}^T \boldsymbol{\eta}_{\mathbf{x}} \right) + \mathcal{O}(h) = 0.$$

By substituting  $\mathbf{v}_{\mathbf{x}} = \boldsymbol{\eta}_{\mathbf{x}}$  in Eq. (17) and simplifying, we obtain

$$(18) \quad (\pi^{d/2} + 2m_2 \rho^2 q) h \partial_{\boldsymbol{\eta}_{\mathbf{x}}} \rho + 2\rho^3 (m_1 q + h m_2 \partial_{\boldsymbol{\eta}_{\mathbf{x}}} q) + \mathcal{O}(h^2) = 0.$$

Substituting  $\mathbf{v}_{\mathbf{x}}^T \boldsymbol{\eta}_{\mathbf{x}} = 0$  in Eq. (17),

$$\pi^{d/2} \frac{\partial_{\mathbf{v}_{\mathbf{x}}} \rho}{\rho} + 2\tilde{m}_2 \rho (q \partial_{\mathbf{v}_{\mathbf{x}}} \rho + \rho \partial_{\mathbf{v}_{\mathbf{x}}} q) + \mathcal{O}(h) = 0.$$

Simplifying the above and substituting the value of  $\tilde{m}_2 = \pi^{d/2}/2$  as defined in Eq. (8), we obtain

$$(1 + \rho^2 q) \partial_{\mathbf{v}_{\mathbf{x}}} \rho + \rho^3 \partial_{\mathbf{v}_{\mathbf{x}}} q + \mathcal{O}(h) = 0.$$

For part (II), we expand Eq. (3) using Lemma 2.1,

$$\begin{aligned}\pi^{d/2} &= \rho \left\{ m_0 \rho q + h m_1 \left( \partial_{\boldsymbol{\eta}_{\mathbf{x}}}(\rho q) + \frac{d-1}{2} H \rho q \right) \right\} + \mathcal{O}(h^2) \\ &= \rho \left\{ \left( m_0 + h m_1 \frac{d-1}{2} H \right) \rho q + h m_1 \partial_{\boldsymbol{\eta}_{\mathbf{x}}}(\rho q) \right\} + \mathcal{O}(h^2) \\ &= \rho q \{ (m_0 + h m_1 \omega) \rho + h m_1 \partial_{\boldsymbol{\eta}_{\mathbf{x}}} \rho \} + \mathcal{O}(h^2)\end{aligned}$$

Rearranging the above equation, we obtain

$$(19) \quad h m_1 \rho q \partial_{\boldsymbol{\eta}_{\mathbf{x}}} \rho = \pi^{d/2} - (m_0 + h m_1 \omega) \rho^2 q + \mathcal{O}(h^2).$$

Multiplying Eq. (18) by  $m_1 \rho q$  and substituting Eq. (19) results in

$$A \rho^4 q^2 - B \rho^2 q + \pi^d = \mathcal{O}(h^2)$$

where, using the definition of  $\omega$  in the statement of the theorem,

$$\begin{aligned}A &= 2 \left( m_1^2 + h m_1 m_2 \frac{\partial_{\boldsymbol{\eta}_{\mathbf{x}}} q}{q} - m_2 (m_0 + h m_1 \omega) \right) \\ &= 2 \left( m_1^2 - m_2 \left( m_0 + \frac{h(d-1)m_1 H}{2} \right) \right)\end{aligned}$$



and, using the definition of  $m_2$  in Eq. (7),

$$B = \pi^{d/2}(m_0 + hm_1\omega - 2m_2) = \pi^{d/2}m_1 \left( h\omega - \frac{2b_{\mathbf{x}}}{h} \right).$$

**Proof of Corollary 2.1.** The proof follows from Eq. (19) by using the fact  $b_{\mathbf{x}} = \infty$  for every point on a closed manifold, and as a result of substituting it in Eq. (5) and (6), we obtain  $m_h^{(0)}(\mathbf{x}) = \pi^{d/2}$  and  $m_h^{(1)}(\mathbf{x}) = 0$ .

**Proof of Corollary 2.2.** We adopt the same notation as in the proof of Theorem 2.1. Due to the assumption  $H = 0$ , we have

$$A = 2(m_1^2 - m_2m_0) \in \left[ -\frac{\pi^{d-1}}{4}(\pi - 1), -\pi^d \right].$$

Consequently,  $B^2 - 4\pi^d A > 0$  and therefore its square root is well defined. For convenience, define  $C_{\pm} := \frac{B \pm \sqrt{B^2 - 4\pi^d A}}{2A}$  and note that  $C_h(\mathbf{x}) = C_-$ . Then, Eq. (9) reduces to

$$(\rho^2 q - C_-)(\rho^2 q + C_+) = \mathcal{O}(h^2).$$

Since  $\rho > 0$ ,  $C_+ < 0$  and

$$C_+ - C_- = \frac{2\sqrt{B^2 - 4\pi^d A}}{2A} \geq \frac{2\pi^{d/2}}{\sqrt{|A|}} \geq 2,$$

therefore  $\rho = C_- + \mathcal{O}(h^2)$ . Since  $\mathcal{M}$  is compact therefore  $C_-$  is bounded and thus  $\rho = C_-(1 + \mathcal{O}(h^2))$ . Finally, if  $\partial_{\eta_{\mathbf{x}}} q$  is also zero then  $\omega = 0$  by definition and the result follows.

**Proof of Corollary 2.3.** Substituting  $b_{\mathbf{x}} = 0$ , we obtain  $m_h^{(0)}(\mathbf{x}) = \frac{\pi^{d/2}}{2}$ ,  $m_h^{(1)}(\mathbf{x}) = -\frac{\pi^{(d-1)/2}}{2}$  and  $m_h^{(2)}(\mathbf{x}) = \frac{\pi^{d/2}}{4}$ .

**Proof of Corollary 2.4.** This follows trivially from Theorem 2.1 by taking away the terms involving  $hH(\mathbf{x})$  and  $h\omega(\mathbf{x})$ .

**Proof of Theorem 3.1.** Using assumption (A6) followed by (A7), we have

$$\boldsymbol{\nu}_i = \frac{1}{n-1} \sum_{j=1}^n \mathbf{W}_{ij} \mathbf{U}_i^T (\mathbf{x}_j + \boldsymbol{\varepsilon}(\mathbf{x}_j) - (\mathbf{x}_i + \boldsymbol{\varepsilon}(\mathbf{x}_i))) = \frac{1}{n-1} \sum_{j=1}^n \mathbf{W}_{ij} \mathbf{U}_i^T (\mathbf{x}_j - \mathbf{x}_i).$$

Using Eq. (4) and the fact that  $\|\mathbf{x}_k\| \leq 1$  and  $\mathbf{U}_i^T \mathbf{U}_i = \mathbb{I}_d$ ,

$$\boldsymbol{\nu}_i = \frac{\rho_h(\mathbf{x}_i)}{\pi^{d/2} h^d} \mathbf{U}_i^T \left( \int k_h(\mathbf{x}_i, \mathbf{y}) \rho_h(\mathbf{y}) (\mathbf{y} - \mathbf{x}_i) q(\mathbf{y}) dV(\mathbf{y}) \right) + \mathcal{O}_{m,n}^{(h)}(g(m, n)).$$

From here on, for brevity, we use the shorthand notation as in the proof of Theorem 2.1. Due to Lemma 2.1 and the product rule for second order derivatives,

$$\frac{1}{h^d} \int k_h(\mathbf{x}, \mathbf{y}) \rho_h(\mathbf{y}) (\mathbf{y} - \mathbf{x}) q(\mathbf{y}) dV(\mathbf{y}) = hm_1 \rho q \boldsymbol{\eta}_{\mathbf{x}} + h^2 \tilde{m}_2 \left( \nabla(\rho q) + \left( \frac{m_2}{\tilde{m}_2} - 1 \right) \partial_{\boldsymbol{\eta}_{\mathbf{x}}}(\rho q) \boldsymbol{\eta}_{\mathbf{x}} \right) + \mathcal{O}(h^3).$$

Denote by  $\partial_{\eta_{\mathbf{x}_\perp}}(\rho q)\boldsymbol{\eta}_{\mathbf{x}_\perp} = \nabla(\rho q) - \partial_{\eta_{\mathbf{x}}}(\rho q)\boldsymbol{\eta}_{\mathbf{x}}$ . Using Theorem 2.1, the r.h.s reduces to,

$$\begin{aligned} & hm_1\rho q\boldsymbol{\eta}_{\mathbf{x}} + h^2(\tilde{m}_2\partial_{\eta_{\mathbf{x}_\perp}}(\rho q)\boldsymbol{\eta}_{\mathbf{x}_\perp} + m_2\partial_{\eta_{\mathbf{x}}}(\rho q)\boldsymbol{\eta}_{\mathbf{x}}) + \mathcal{O}(h^3) \\ &= hm_1\rho q\boldsymbol{\eta}_{\mathbf{x}} + h^2(\tilde{m}_2\partial_{\eta_{\mathbf{x}_\perp}}(\rho q)\boldsymbol{\eta}_{\mathbf{x}_\perp} + m_2(\rho\partial_{\eta_{\mathbf{x}}}q + q\partial_{\eta_{\mathbf{x}}}\rho)\boldsymbol{\eta}_{\mathbf{x}}) + \mathcal{O}(h^3) \\ &= h\left(m_1\rho q - \frac{2m_1m_2\rho^3q^2}{\pi^{d/2} + 2m_2\rho^2q}\right)\boldsymbol{\eta}_{\mathbf{x}} + h^2\left(\tilde{m}_2\partial_{\eta_{\mathbf{x}_\perp}}(\rho q)\boldsymbol{\eta}_{\mathbf{x}_\perp} + m_2\left(\rho\partial_{\eta_{\mathbf{x}}}q - \frac{2m_2\rho^3q\partial_{\eta_{\mathbf{x}}}q}{\pi^{d/2} + 2m_2\rho^2q}\right)\boldsymbol{\eta}_{\mathbf{x}}\right) + \mathcal{O}(h^3) \\ &= h\left(\frac{\pi^{d/2}m_1\rho q}{\pi^{d/2} + 2m_2\rho^2q}\right)\boldsymbol{\eta}_{\mathbf{x}} + h^2\left(\tilde{m}_2\partial_{\eta_{\mathbf{x}_\perp}}(\rho q)\boldsymbol{\eta}_{\mathbf{x}_\perp} + \frac{\pi^{d/2}m_2\rho\partial_{\eta_{\mathbf{x}}}q}{\pi^{d/2} + 2m_2\rho^2q}\boldsymbol{\eta}_{\mathbf{x}}\right) + \mathcal{O}(h^3) \end{aligned}$$

From Theorem 2.1, if  $\mathbf{v}_{\mathbf{x}} \perp \boldsymbol{\eta}_{\mathbf{x}}$  then

$$\partial_{\mathbf{v}_{\mathbf{x}}}(\rho q) = (\rho\partial_{\mathbf{v}_{\mathbf{x}}}q + q\partial_{\mathbf{v}_{\mathbf{x}}}\rho) = \left(\rho\partial_{\mathbf{v}_{\mathbf{x}}}q - \frac{\rho^3q\partial_{\mathbf{v}_{\mathbf{x}}}q}{1 + \rho^2q}\right) + \mathcal{O}(h) = \frac{\rho\partial_{\mathbf{v}_{\mathbf{x}}}q}{1 + \rho^2q} + \mathcal{O}(h).$$

Using the above equation and Corollary 2.4 (which also shows  $\rho^2q = \mathcal{O}(1)$ ), the r.h.s. reduces to,

$$\begin{aligned} & h\left(\frac{\pi^{d/2}m_1\rho q}{\pi^{d/2} + 2m_2\rho^2q}\right)\boldsymbol{\eta}_{\mathbf{x}} + \frac{h^2\pi^{d/2}\rho}{2}\left(\frac{\partial_{\eta_{\mathbf{x}_\perp}}q}{1 + \rho^2q}\boldsymbol{\eta}_{\mathbf{x}_\perp} + \frac{2m_2\partial_{\eta_{\mathbf{x}}}q}{\pi^{d/2} + 2m_2\rho^2q}\boldsymbol{\eta}_{\mathbf{x}}\right) + \mathcal{O}(h^3) \\ &= \frac{h}{\rho}\left(\frac{\pi^{d/2}m_1\zeta}{\pi^{d/2} + 2m_2\zeta}\right)\boldsymbol{\eta}_{\mathbf{x}} + \mathcal{O}(h^2). \end{aligned}$$

Using the definition of  $\beta_h$  in the statement of the theorem and the fact that  $\mathcal{U}_i^T\boldsymbol{\eta}_{\mathbf{x}_i} = \boldsymbol{\eta}_{\mathbf{x}_i}$ , we obtain the result.

#### ACKNOWLEDGMENTS

This work was partially funded by NSF award 2217058. CH also wishes to acknowledge an award from the W.M. Keck foundation.

#### REFERENCES

- [1] T. BERRY AND T. SAUER, *Density estimation on manifolds with boundary*, Computational Statistics & Data Analysis, 107 (2017), pp. 1–17.
- [2] KOHLI, DHURV, A. CLONINGER, AND G. MISHNE, *LDLE: Low Distortion Local Eigenmaps*, Journal of Machine Learning Research, 22 (2021), pp. 1–64.
- [3] KOHLI, DHURV, J. S. NIEUWENHUIS, A. CLONINGER, G. MISHNE, AND D. NARAIN, *RATS: Unsupervised manifold learning using low-distortion alignment of tangent spaces*, bioRxiv, (2024).
- [4] J. M. BORWEIN, A. S. LEWIS, AND R. D. NUSSBAUM, *Entropy minimization, DAD problems, and doubly stochastic kernels*, Journal of Functional Analysis, 123 (1994), pp. 264–307.
- [5] J. CALDER, *Graphlearning python package*, Jan. 2022, <https://doi.org/10.5281/zenodo.5850940>, <https://doi.org/10.5281/zenodo.5850940>.
- [6] J. CALDER, S. PARK, AND D. SLEPČEV, *Boundary estimation from point clouds: Algorithms, guarantees and applications*, Journal of Scientific Computing, 92 (2022), <https://doi.org/10.1007/s10915-022-01894-9>.
- [7] M.-Y. CHENG AND H.-T. WU, *Local linear regression on manifolds and its geometric interpretation*, Journal of the American Statistical Association, 108 (2013), pp. 1421–1434.
- [8] X. CHENG AND B. LANDA, *Bi-stochastically normalized graph laplacian: convergence to manifold laplacian and robustness to outlier noise*, Information and Inference: A Journal of the IMA, 13 (2024), p. iaee026.
- [9] R. R. COIFMAN AND S. LAFON, *Diffusion maps*, Applied and computational harmonic analysis, 21 (2006), pp. 5–30.
- [10] M. CUTURI, *Sinkhorn distances: Lightspeed computation of optimal transport*, Advances in neural information processing systems, 26 (2013).
- [11] D. GONG, F. SHA, AND G. MEDIONI, *Locally linear denoising on image manifolds*, in Proceedings of the Thirteenth International Conference on Artificial Intelligence and Statistics, JMLR Workshop and Conference Proceedings, 2010, pp. 265–272.
- [12] M. JONES AND P. FOSTER, *A simple nonnegative boundary correction method for kernel density estimation*, Statistica Sinica, (1996), pp. 1005–1013.

- [13] P. W. JONES, M. MAGGIONI, AND R. SCHUL, *Universal local parametrizations via heat kernels and eigenfunctions of the Laplacian*, arXiv preprint arXiv:0709.1975, (2007).
- [14] A. JUNG AND M. HULSEBOS, *The network nullspace property for compressed sensing of big data over networks*, *Frontiers in Applied Mathematics and Statistics*, 4 (2018), p. 9.
- [15] R. J. KARUNAMUNI AND T. ALBERTS, *On boundary correction in kernel density estimation*, *Statistical Methodology*, 2 (2005), pp. 191–212.
- [16] P. KNOPP AND R. SINKHORN, *A note concerning simultaneous integral equations*, *Canadian Journal of Mathematics*, 20 (1968), pp. 855–861.
- [17] B. LANDA AND X. CHENG, *Robust inference of manifold density and geometry by doubly stochastic scaling*, *SIAM Journal on Mathematics of Data Science*, 5 (2023), pp. 589–614.
- [18] B. LANDA, R. R. COIFMAN, AND Y. KLUGER, *Doubly stochastic normalization of the gaussian kernel is robust to heteroskedastic noise*, *SIAM journal on mathematics of data science*, 3 (2021), pp. 388–413.
- [19] J. M. LEE, *Introduction to Riemannian manifolds*, vol. 2, Springer, 2018.
- [20] N. F. MARSHALL AND R. R. COIFMAN, *Manifold learning with bi-stochastic kernels*, *IMA Journal of Applied Mathematics*, 84 (2019), pp. 455–482.
- [21] L. MCINNES, J. HEALY, AND J. MELVILLE, *Umap: Uniform manifold approximation and projection for dimension reduction*, arXiv preprint arXiv:1802.03426, (2018).
- [22] K. MOHAMMED AND H. NARAYANAN, *Manifold learning using kernel density estimation and local principal components analysis*, arXiv preprint arXiv:1709.03615, (2017).
- [23] E. F. SCHUSTER, *Incorporating support constraints into nonparametric estimators of densities*, *Communications in Statistics-Theory and methods*, 14 (1985), pp. 1123–1136.
- [24] A. SINGER AND H.-T. WU, *Vector diffusion maps and the connection laplacian*, *Communications on pure and applied mathematics*, 65 (2012), pp. 1067–1144.
- [25] R. VAUGHN, T. BERRY, AND H. ANTIL, *Diffusion maps for embedded manifolds with boundary with applications to pdes*, arXiv preprint arXiv:1912.01391v2, (2019), <https://arxiv.org/pdf/1912.01391v2>.
- [26] R. VAUGHN, T. BERRY, AND H. ANTIL, *Diffusion maps for embedded manifolds with boundary with applications to PDEs*, *Applied and Computational Harmonic Analysis*, 68 (2024), p. 101593, <https://doi.org/https://doi.org/10.1016/j.acha.2023.101593>, <https://www.sciencedirect.com/science/article/pii/S1063520323000805>.
- [27] Y. YU, T. WANG, AND R. J. SAMWORTH, *A useful variant of the davis-kahan theorem for statisticians*, *Biometrika*, 102 (2015), pp. 315–323.

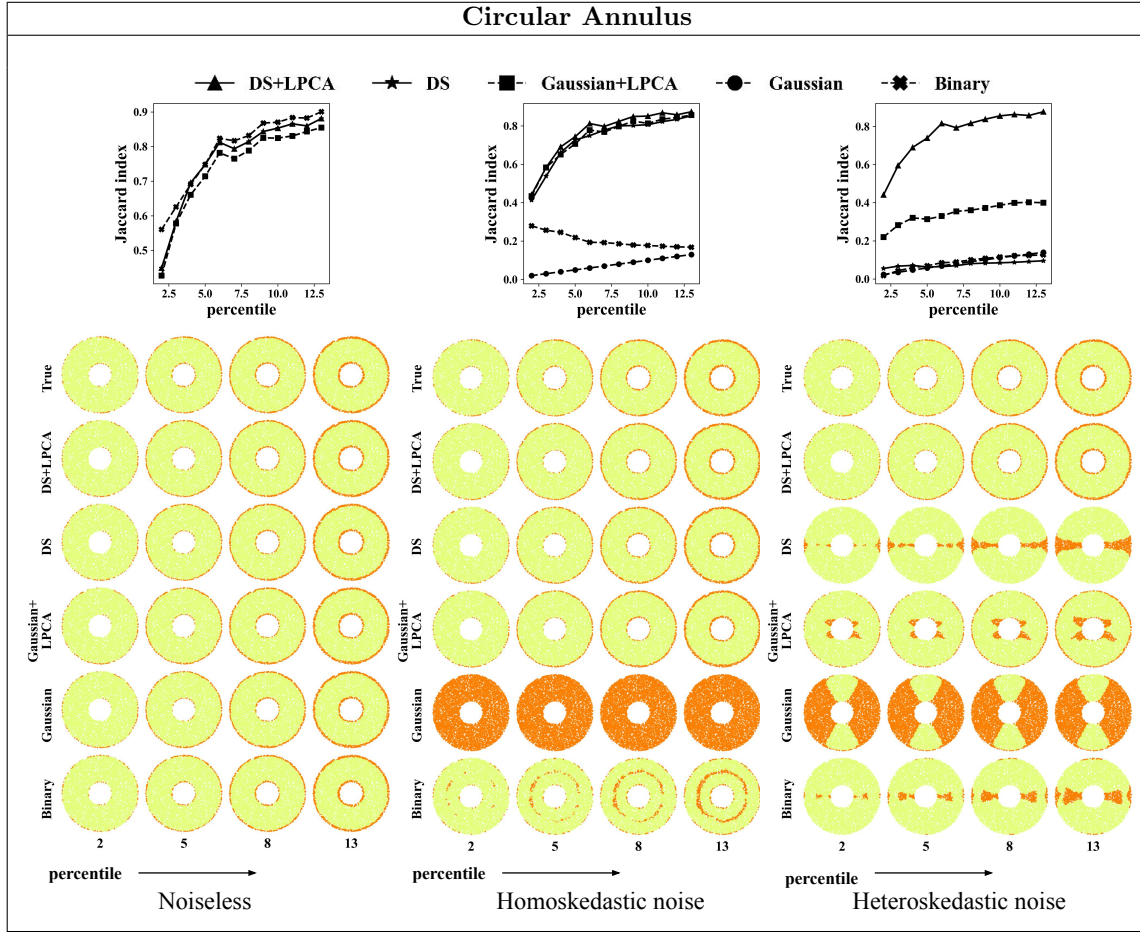


FIGURE 4. (Top) The Jaccard index (Eq. (16)) is shown between the ground truth  $p$ -th percentile boundary  $\mathcal{B}_p$  and the estimated  $p$ -th percentile boundary  $\hat{\mathcal{B}}_p$  for  $p \in [2, 14]$ . (Bottom) Visualizations of the boundaries  $\mathcal{B}_p$  and  $\hat{\mathcal{B}}_p$  (in orange) are provided for competing methods at  $p \in \{2, 5, 8, 11\}$ .

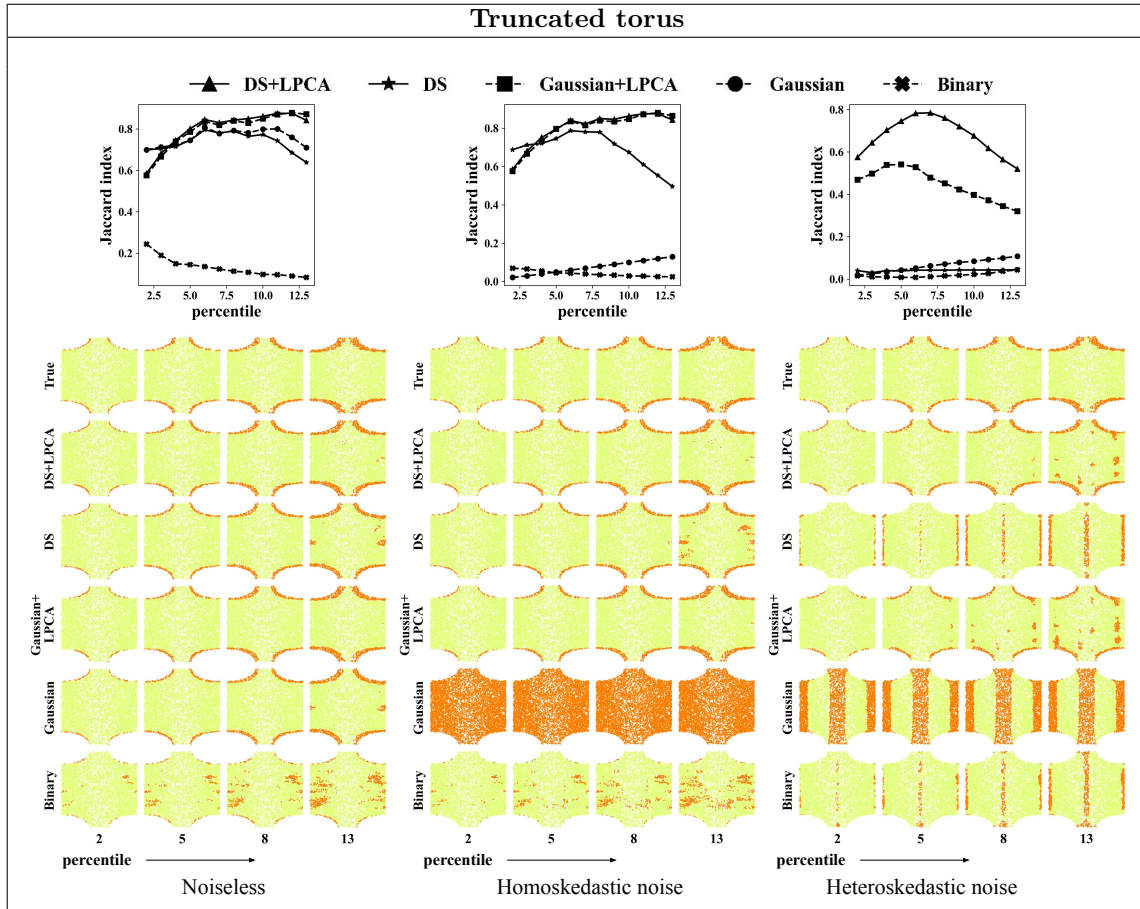


FIGURE 5. (Top) The Jaccard index (Eq. (16)) is shown between the ground truth  $p$ -th percentile boundary  $\mathcal{B}_p$  and the estimated  $p$ -th percentile boundary  $\hat{\mathcal{B}}_p$  for  $p \in [2, 14]$ . (Bottom) Visualizations of the boundaries  $\mathcal{B}_p$  and  $\hat{\mathcal{B}}_p$  (in orange) are provided for competing methods at  $p \in \{2, 5, 8, 11\}$ . The visualizations are presented on the two-dimensional domain of the truncated torus.

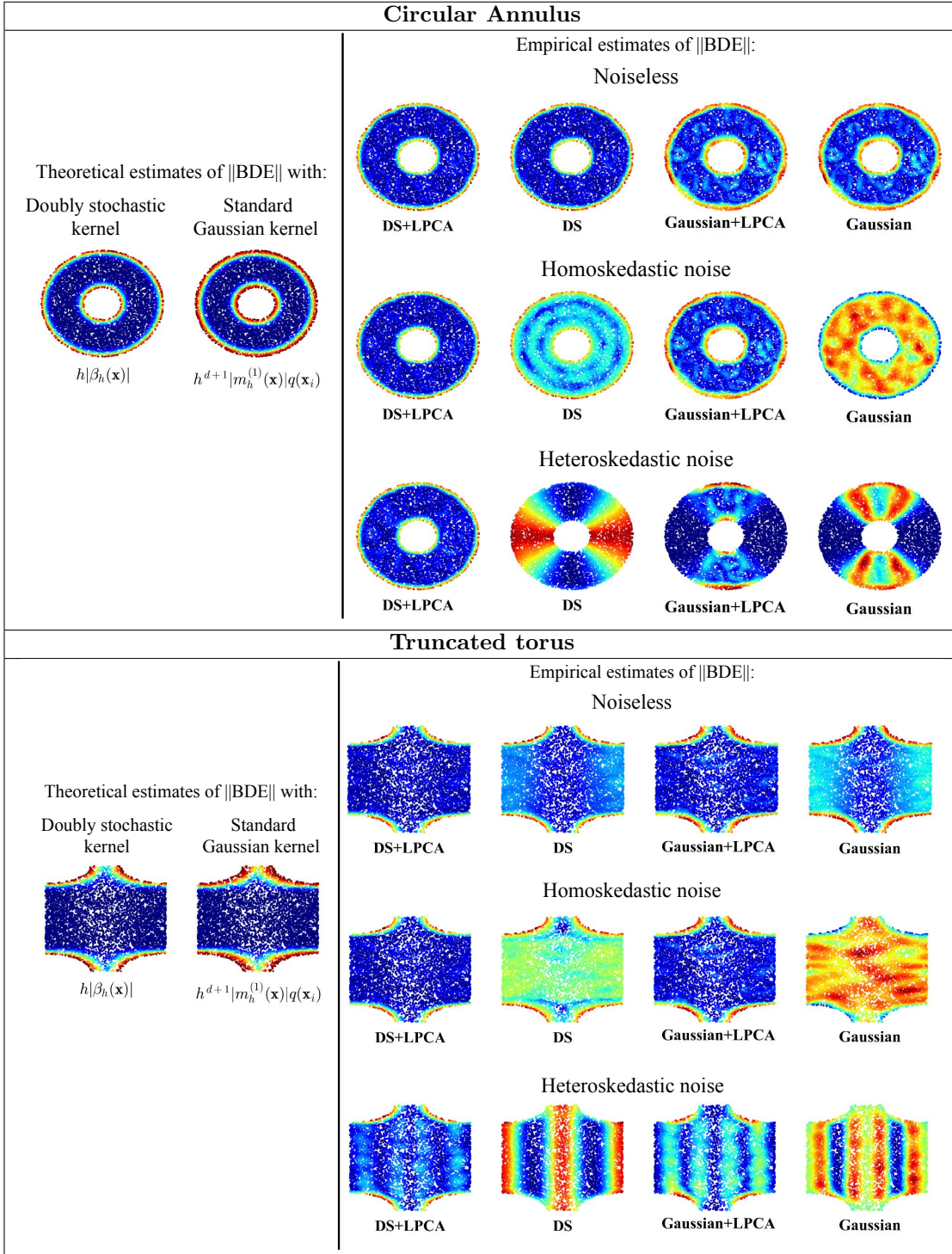


FIGURE 6. (Left) The theoretical norm of the BDE, as in Eq. (11) and Eq. (13), at each point on the data manifold are visualized. These are computed using the true distances to the boundary and the assumption that  $q$  is uniform. (Right) The empirical norm of the BDE due to each method, as in Eq. (10) and Eq. (12), are visualized on the data manifold. For consistency, the values for each fixed dataset and method are normalized by their maximum so that they range between 0 and 1. For the truncated torus, the visualizations are presented onto its two-dimensional domain.



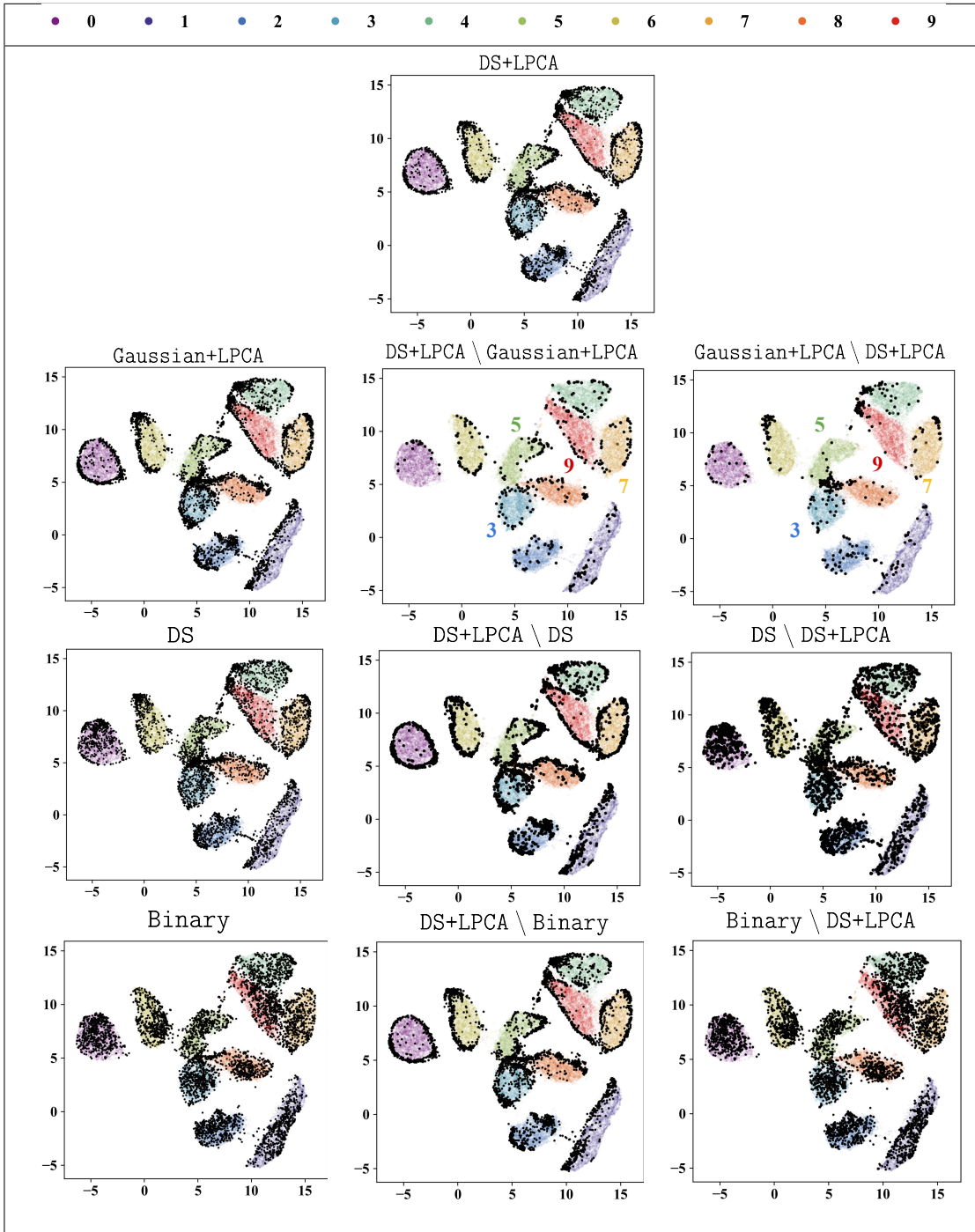
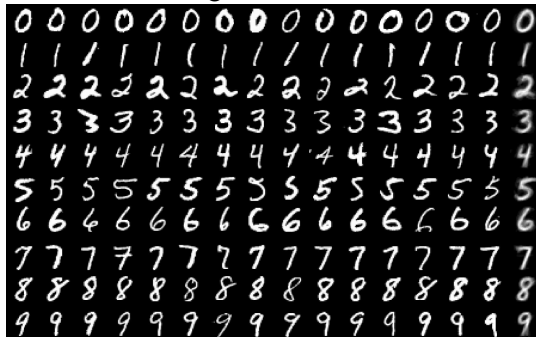


FIGURE 7. The 10-th percentile boundary  $\hat{\mathcal{B}}_{10}$  (as defined in Eq. (15)) is estimated from 5000 raw  $28 \times 28$  images of each MNIST digit using DS+LPCA, Gaussian + LPCA, DS and Binary. The visualizations are presented on a two-dimensional UMAP[21] embedding of the data, where points in  $\hat{\mathcal{B}}_{10}$  are highlighted in black. These plots show points on the estimated boundaries due to each method, the ones that lie on the estimated boundaries by two of the methods, and by one method but not the other.

DS+LPCA : images in the interior



DS+LPCA : images near the boundary



FIGURE 8. A random selection of 15 images per digit is shown, including those from the interior of the MNIST dataset (outside  $\hat{\mathcal{B}}_{95}$ ) and near the boundary (inside  $\hat{\mathcal{B}}_5$ ), as estimated using DS + LPCA. The final column displays the average of the 15 images.